Princeton Plasma Physics Laboratory

PPPL- 5019

PPPL- 5019

Quasilinear Carbon Transport In An Impurity Hole Plasma In LHD

David Mikkelsen, et. al.

APRIL, 2014

PPPL PRINCETON PLASMA PHYSICS LABORATORY

Prepared for the U.S. Department of Energy under Contract DE-AC02-09CH11466.

Princeton Plasma Physics Laboratory
Report Disclaimers

Full Legal Disclaimer

Trademark Disclaimer

PPPL Report Availability

Princeton Plasma Physics Laboratory:

http://www.pppl.gov/techreports.cfm

Office of Scientific and Technical Information (OSTI):

http://www.osti.gov/bridge

Related Links:

U.S. Department of Energy

Office of Scientific and Technical Information

Fusion Links

Quasilinear Carbon Transport in an Impurity Hole Plasma in LHD

D.R. Mikkelsen,[1, a)] K. Tanaka,[2] M. Nunami,[2] T.-H. Watanabe,[3] H. Sugama,[2] M. Yoshinuma,[2] K. Ida,[2] Y. Suzuki,[2] M. Goto,[2] S. Morita,[2] B. Wieland,[2] I. Yamada,[2] R. Yasuhara,[2] T. Tokuzawa,[2] T. Akiyama,[2] and N. A. Pablant[1]

[1)] *Princeton Plasma Physics Laboratory*

[2)] *National Institute for Fusion Science, 322-6 Oroshi, Toki, Gifu 509-5292, Japan*

[3)] *Department of Physics, Nagoya University Furo-cho, Chikusa-ku, Nagoya 464-8602, Japan*

(Dated: Draft on 22 April 2014)

Comprehensive electrostatic gyrokinetic linear stability calculations for ion-scale microinstabilities in an LHD plasma with an ion-ITB and carbon 'impurity hole' are used to make quasilinear estimates of particle flux to explore whether microturbulence can explain the observed outward carbon fluxes that flow 'up' the impurity density gradient. The ion temperature is not stationary in the ion-ITB phase of the simulated discharge, during which the core carbon density decreases continuously. To fully sample these varying conditions the calculations are carried out at three radial locations and four times. The plasma parameter inputs are based on experimentally measured profiles of electron and ion temperature, as well as electron and carbon density. The spectroscopic line-average ratio of hydrogen and helium densities is used to set the density of these species. Three ion species (H,He,C) and the electrons are treated kinetically, including collisions. Electron instability drive does enhance the growth rate significantly, but the most unstable modes have characteristics of ion temperature gradient (ITG) modes in all cases. As the carbon density gradient is scanned between the measured value and zero, the quasilinear carbon flux is invariably inward when the carbon density profile is hollow, so turbulent transport due to the instabilities considered here does not explain the observed outward flux of impurities in impurity hole plasmas. The stiffness of the quasilinear ion heat flux is found to be 1.7-2.3, which is lower than several estimates in tokamaks.

PACS numbers: 52.65.Tt, 52.25.Vy, 52.25.Fi, 52.35.Qz, 52.55.Hc

[a)]Electronic mail: dmikkelsen@pppl.gov

I. INTRODUCTION

The observation of extremely 'hollow' impurity density profiles, or 'impurity holes', has been reported in plasmas with a steep ion temperature gradient[1–7] in the heliotron-type Large Helical Device (LHD)[8]. Extremely hollow profiles have been observed for carbon[1,2] and neon[3], but not for helium[3]. Detailed profile information is not available for argon, but a strong drop in the concentration of argon has also been reported[2]. Recent experiments have also observed impurity holes in low density L-mode plasmas in LHD[9]. The electron density in these experiments is similar to i-ITB plasmas, but the heating power and both temperatures are much lower.

The outflux of impurities from the plasma core is very favorable for fusion because it reduces dilution of reacting fuel species and radiative energy losses from the plasma core, so it is important to understand the transport mechanism responsible for it. Although less dramatically hollow impurity density profiles are also observed in electron-ITB plasmas (in the electron-root regime), impurity holes only occur in plasmas heated by neutral beam injection. They are most commonly observed conjunction with an ion 'internal transport barrier' (ITB), a broad region of reduced ion thermal diffusivity, and have been associated with elevated ion temperature gradients[1].

Standard treatments of neoclassical transport predict an inward impurity flux in the i-ITB conditions[2,4], and they predict more generally that the ion-root regime in stellarators will always produce inward impurity fluxes[10]. There is, however, an inconsistency in these calculations that is important for medium- to high-Z impurities. The electrostatic potential is predicted to have poloidal variation that will contribute to the radial drift, but this is ignored. For low Z ions this neglected drift is small compared to the curvature and $\nabla|B|$ drifts, but it is proportional to the particle charge so it could be important for carbon and higher-Z impurities[11]. Initial calculations that include variations of the neoclassical electrostatic potential within each flux surface indicate that it can affect significantly the impurity particle fluxes and in some cases produce outward impurity flux in the ion-root regime in the LHD configuration[12], but the density and temperature profiles assumed in Ref. 12 are much more collisional than those of the impurity hole regime. Recent calculations with parameters much closer to impurity hole conditions have not produced results that can explain the outward fluxes that create the impurity hole[13] but the method of calculation is

still under development.

The neoclassical calculations made to date have predicted that the plasma is in the 'ion root' regime at all radii, but the experimental picture is more complex. Direct measurement of the plasma potential by a heavy ion beam probe confirm that the radial electric field is negative for r/a <0.55[4,5], but measured flow speeds require that the the radial electric field is positive in the outer ∼15-20% of the minor radius. Large flows are not included in standard stellarator neoclassical calculations (which assume that toroidal flows are heavily damped), so the neoclassical expectation is not relevant near the plasma edge. The steeply hollow part of the carbon density profile occurs where there is no measurement that could determine the sign of the radial electric field, but if it is positive that might explain the impurity hole.

It is also possible that turbulent transport could produce the impurity hole. The carbon density is observed to be peaked until the rising ion temperature gradient apparently triggers the impurity outflux[1]. Pioneering studies found that toroidal drift modes are unstable in the outer region of several types of LHD plasmas[14]. In addition, quasilinear estimates of the turbulent electron particle flux in other types of low-density LHD plasmas have been used to explain why some of these plasmas have mildly hollow electron density profiles[15,16]. More recent studies of impurity hole plasmas find that ion temperature gradient (ITG) modes are linearly unstable[17], and nonlinear turbulence simulations indicate that ITG turbulence produces the level of 'anomalous' heat flux needed to augment the neoclassical flux and balance the ion heating[18].

We report the first gyrokinetic calculations of impurity transport in a heliotron or stellarator, and explore whether microturbulent transport could explain the observed outward carbon flux in the impurity hole regime. Our quasilinear heat and particle fluxes are based on comprehensive calculations of linear stability with three kinetic ion species - hydrogen, helium and carbon - and a kinetic treatment of electrons that includes finite collisionality. Electromagnetic modes are not included because the β of the impurity hole plasmas is not large, but the possibility that they may contribute to the carbon transport can't be ruled out until this is studied. Electron scale modes, i.e. $k_{\mathrm{y}}\rho_{\mathrm{i}}$ >2, have not been examined because gyro-averaging can be expected to reduce ion particle fluxes to very small levels, and this is confirmed in the present study for modes with $k_{\mathrm{y}}\rho_{\mathrm{i}}$ ∼2-3.

The experimental conditions are described in Section II, with a focus on the dynamics

of the carbon density and the ion temperature. In Section III we describe the gyrokinetic calculations, and summarize the resolution convergence tests and the mode identification studies. Electron instability drive terms are included and they enhance the growth rates significantly, but at all four times and all three radii studied here, we find that the most unstable modes are ITG modes. The effect of the variations of the carbon density and the ion temperature on the linear stability are discussed in Section IV. Quasilinear estimates of the carbon particle flux are compared with experimental transport analysis in Section V. All the examined modes produce inward carbon fluxes for hollow carbon profiles, so the quasilinear estimates of carbon flux can not explain the observed outward flux of impurities when the impurity density profile is hollow.

The linear stability calculations described below are sufficient to produce quasilinear estimates of the stiffness of the turbulent ion heat transport, a topic of growing interest[19]. In Section VI we derive estimates of the ion stiffness of an LHD impurity hole plasma, and all the results are summarized in Section VII.

II. CHARACTERISTICS OF AN IMPURITY HOLE PLASMA

The calculations reported here are based on measurements of LHD high-T_i discharge 113208, with a nominal magnetic axis located at 3.6 m, a minor radius of 0.63 m, toroidal magnetic field of 2.75 T. LHD plasmas with steep ion temperature gradients and extremely hollow impurity density profiles are created in low density plasmas heated by *both* N-NBI and P-NBI. At the times simulated below the plasma is heated by ∼14 MW of neutral beam injection with high energy beams at 180 keV (with negative ion sources: N-NBI), and ∼10.5 MW of low energy beams at 40 keV (with positive ion sources: P-NBI). The modulated P-NB used for the ion temperature measurement (with 4.5 MW) begins at 4.6 sec, and another 6 MW of P-NBI is injected continuously during the interval containing the simulation times. The first P-NB is turned on at 4.0 sec and the emission from Ar^{+16} measured by the XICS diagnostic[20] indicates that the emissivity profile has become hollow by 4.2 sec, but the signal strength is not sufficient to enable an accurate inversion of these line-integrated measurements. A strong drop in the concentration of argon has been reported before[2] using different instruments, but some of the central emissivity reduction in each case is likely to be caused by high-temperature 'burn out' of the Ar^{+16} charge state. The XICS

data indicate that the Ar^{+16} emission is strongly centrally peaked shortly after t=4.0 sec, but this ends as the central T_e enters the region of Ar^{+16} burnout. The argon density profile may be hollow during the period of the carbon impurity hole, but the available data are not sufficient to settle the issue. The argon concentration is low, so reliable profile measurements of the ion temperature and the carbon density (based on charge-exchange between carbon ions and injected neutral hydrogen) begin with the addition of the second P-NBI at 4.6 sec (Fig. 1); its power is modulated to improve the background subtraction.

At 4.55 sec a plastic pellet is injected in order to raise the carbon content and thereby increase the signal strength of the charge-exchange recombination spectroscopy (CXRS) system with an absolutely calibrated spectrometer that measures carbon density, temperature, and rotation speed based on analysis of the (n=8→7) line of carbon CVI that is produced by charge-exchange with the neutral hydrogen atoms injected by the P-NBI. See Refs. 1 and 21 (and references cited therein) for a detailed discussion of the analysis of the charge exchange spectra. The density provided by pellet injection decays quickly, so the electron density is relatively steady across the four simulation times (Fig. 1).

In order to achieve high ion temperature, edge recycling and the plasma density near the edge were reduced by making a series of helium-majority wall conditioning discharges with H-minority ICRH-only heating[7]. Consequently, the helium density fraction is relatively high in the i-ITB discharges, n_{He}/n_e ~15-20%, so hydrogen and helium are both included in the gyrokinetic calculations.

The calculations in following sections are based on measured electron and ion temperature profiles, electron and carbon density profiles, and the line-average ratio of hydrogen and helium densities obtained spectroscopically[22,23]. These define the needed ratios of ion to electron density, ion to electron temperature, and normalized gradient scale lengths of the ion and electron temperatures and densities. All ion species are assumed to have the same temperature as that measured for the carbon ions. A VMEC 3D equilibrium is used to map all profile measurements to a common minor radius coordinate, $r_{eff} = a\sqrt{s}$, where s is VMEC's normalized toroidal flux coordinate. The normalized coordinate r/a used in figures and text is $r/a = \sqrt{s}$.

The electron density and temperature is measured by a Thomson-scattering system based on a yttrium aluminum garnet (YAG) laser[24]. The electron density is also measured by a Far-Infrared Laser Interferometer (FIR)[25]; both electron density measurements are in good

agreement at the simulation locations. Figs. 2 and 3 show that the full profiles of electron density and temperature change very little at the simulation times.

The measured carbon temperature (Fig. 4) and density (Fig. 5) are quite variable, so the four simulation times have been selected to include extreme and typical values. At t=4.64 sec the carbon density is still high, while at t=4.74 sec the ion temperature and its gradient scale length parameter are near their respective maxima and the carbon density is only mildly hollow. At t=4.84 and 4.94 sec the carbon density is small and very hollow while the ion temperature is fairly steady but lower than at earlier times. The ion temperature has already risen substantially at t=4.64 sec and it continues to rise until ∼4.7 sec, followed by more gradual reduction and it becomes nearly stationary by 4.84 seconds. Deep in the core the outward flow of carbon persists from the time when the core carbon density is still high to late times when the profile very hollow. The outer part of the carbon density profile, $r/a >$0.7, becomes nearly stationary after 4.7 sec. The carbon density is least hollow around the time of peak ion temperature, but the carbon density gradient parameter is negative at all the simulation radii and times.

Helium and carbon are close to fully ionized throughout the plasma core, so the measured electron and carbon densities constrain the weighted sum of the hydrogen and helium densities to be given by

$$n_{\mathrm{H}} + 2n_{\mathrm{He}} = n_{\mathrm{e}} - 6n_{\mathrm{C}}.$$

The relative densities of hydrogen and helium are assumed to be radially uniform, and to match the the line averaged ratio of hydrogen and helium ion densities estimated from absolutely calibrated spectroscopic measurements[22], where

$$\frac{n_{\mathrm{H}}}{(n_{\mathrm{H}} + n_{\mathrm{He}})} \sim 0.75$$

at all four simulation times. The Z_{eff} used in the simulations is derived from the measured and inferred densities of hydrogen, helium, and carbon.

The presence of turbulence is indicated by electron density fluctuations measured by a 10.6 μm CO_2 laser two-dimensional phase contrast imaging system (2D-PCI)[26,27]. The measured wavenumber and frequency ranges are 0.1–1 mm^{-1} and 20–500 kHz, appropriate for ITG/TEM ion-scale turbulence. The measured k component is dominantly poloidal, so the poloidal propagation direction in the laboratory frame can be measured. The radial location of the turbulence is determined by magnetic field orientation using the assumption

that the density fluctuation's $k_\perp \gg k_\parallel$, so propagation is perpendicular to the magnetic field. The magnetic field changes direction monotonically along the vertically injected laser beam so the propagation direction uniquely identifies the local position, allowing coverage of the plasma above and below the equatorial plane.

The top panel of Figs. 6 and 7 shows the fluctuation amplitude profile, which is integrated over k and frequency. The ion and electron diamagnetic propagation components in the laboratory frame are shown separately. The second panel shows the spatial profile of the wavenumber spectrum. The third panel shows the spatial profile of fluctuation phase velocity in the laboratory frame. The color bar indicates fluctuation amplitude on a logarithmic scale. In Figs. 6 and 7 positive and negative $\rho = r_{\rm eff}/a$ indicate the upper and lower halves of the plasma. The CXRS system measures the $E_r \times B_{tor}$ poloidal rotation velocity projected onto the PCI detector plane; this is shown by the light blue data symbols in the third panel.

At all four times, the fluctuation intensity peaks near $\rho \sim$0.7, sometimes extending over ρ =0.4–1.1. The wavenumber spectra peak near 0.25 mm^{-1} for $\rho \sim$0.7, which corresponds to $k_\perp \rho_{\rm i} \sim$0.4. However, this peak is likely to be influenced by instrumental cut off, so the real peak is at smaller $k_\perp \rho_{\rm i}$, or larger spatial scales. The strongest fluctuations propagate in the ion diamagnetic direction in the laboratory frame. The phase velocity in the laboratory frame is almost constant in time, but is not well separated from the $E_r \times B_{tor}$ rotation so the propagation direction in the plasma frame is indeterminate.

The spatial profile of the fluctuation amplitude is up/down symmetric at t=4.64 sec, but for t=4.74 sec and later times it is consistently up/down asymmetric. The origin of the observed asymmetry is not understood. Up-down asymmetries do not appear in linear or nonlinear turbulence simulations of these plasmas. A misaligned focusing lens could cause asymmetries, but if the asymmetry is an instrumental effect, it should be seen at all times. The observed asymmetry, however, changes in time during a single shot and is observed to do so in other discharges as well, so the asymmetry's cause probably lies in the plasma. The fluctuation amplitude in the upper plasma is almost constant in time, but in the lower region the fluctuation amplitude changes in time: increasing from t=4.64 sec to t=4.74 sec, then staying constant till t=4.97 sec. Throughout the four simulation times, the electron density is nearly constant (Figs. 2), so the evolution of relative fluctuation level, $\tilde{n}/n_{\rm e}$, is the same as the fluctuation amplitude.

III. CALCULATION METHODS, CONVERGENCE, AND MODE IDENTIFICATION

The calculations reported here were carried out with GS2, a gyrokinetic Vlasov code with a comprehensive treatment of effects thought to be important for turbulence in the core of toroidal plasmas, including multiple species, fully kinetic descriptions of all species, and collisions[28,29]. It is also capable of treating fully electromagnetic fluctuations and sheared flows, but these features are not included in the electrostatic simulations reported here. Turbulence suppression by $E \times B$ shear cannot be properly accounted for in linear gyrokinetic calculations, but their is no reason to think it would influence the sign of the radial flux of carbon in a nonlinear calculation. The original geometrical capabilities for non-circular tokamaks were extended to three-dimensional, non-axisymmetric devices and benchmarked[30,31] for an NCSX equilibrium against the FULL code[32], the GENE code[33,34], and GKV-X[35]. For the calculations reported below, the local flux-tube geometry employed[36] in GS2 is based on configuration information extracted by VVBAL[37] (as part of the GIST code[38]) from an MHD equilibrium calculated by VMEC[39].

Since $\beta_{\rm tot}$ is nearly constant (0.6-0.75%) at the simulations times, a single VMEC calculation is used for all simulation times. The pressure profile shape is $\propto (1-(r/a)^2)^2$; the magnitude is based on the kinetic pressure, then adjusted to align the flux surfaces with the measured $T_{\rm e}$ profile. The internal toroidal current of 65 kA is derived from magnetic measurements and has an assumed profile shape $\propto (1-(r/a)^2)^2$, which is representative of centrally peaked neutral beam driven current in a low density plasma with strong central deposition. The plasma boundary is fixed to the calculated vacuum boundary. In terms of the VMEC equilibrium used here, the field line that is the basis for the flux tube geometry has $\alpha_{\rm o} = \pi/10$ and $\theta_{\rm o} = 0$ because this maximizes the growth rate. In more physical terms, this places the middle of the theta domain (theta=0) at the outer midplane where the plasma cross section is elongated horizontally.

Measurements of the electron and ion temperature profiles, electron and carbon density profiles, and the line-averaged ratio of the hydrogen and helium densities provide the plasma parameters needed for the calculations. These parameters take on non-measured values only in parameter scans and sensitivity studies. The electron collision model includes electron-electron and electron-ion collisions, and all the inferred ion densities are used to calculate

the electron-ion collision rate. The ion-ion collision rate is set to zero in most calculations to save time; the error is small, as discussed below.

Linear and quasilinear properties of the fastest growing eigenmode are calculated independently (and simultaneously, in parallel operation) for each specified perpendicular wavenumber with a time-implicit initial-value finite-difference algorithm in the ballooning (or "flux-tube") limit. The perpendicular wavenumber used in GS2 is dimensionless, normalized by the inverse gyro-radius of the majority ion (hydrogen here). The values of the wavenumber spectrum ($k_{\rm y}\rho_{\rm i}$=0.2,0.28,0.4,0.6,0.9,1.35) are chosen to extend below and above the peak growth rates and peak quasilinear fluxes (See Figs. 10-17). Grid resolution convergence studies were carried out for each radial location and simulation time. The convergence and mode identification studies reported next focus on changes in the growth rates of the most important modes, with $k_{\rm y}\rho_{\rm i}$=0.3-0.6.

The standard grid spacing for θ, the coordinate aligned with the magnetic field, is $\Delta\theta =$ 0.01, which places ∼35 grid points across each local ripple well at r/a=0.6 (Fig. 8). The domain extends to $\theta = \pm 9.15$ radians, and one can see in Fig. 9 that the eigenfunctions have become small far from the ends of the domain. The eigenfunction shape has a 'ballooning' character that is typical of ITG modes in both tokamaks and stellarators, and the width extends over many local ripple wells. With twice the usual step size, $\Delta\theta = 0.02$, the growth rates change by 1% or less. Gaussian integration techniques are used for velocity space integrals, so these converge with relatively sparse grids. Our production runs use 8 energies; with twice as many the growth rates change by 1% or less. The standard number of trapped pitch angles is 35 (far more than typically used for tokamak calculations); when this is raised to 46 the growth rates change by not more than 2%. The normalized time step, $\Delta t(v_{\rm i}/a)$, is 0.05; when reduced to 0.02 the growth rates change by up to 3%. The ion-ion collision rate is set to zero in most runs; when the experimental values are used the growth rates change by 1% or less.

Mode identification studies show that the fastest growing modes are ITG modes at each radial location and simulation time. When the main ITG driver, $a/L_{\rm Ti}$, is changed by ±20% the growth rates change by ±15-25%. However, when $a/L_{\rm Te}$ (an important drive term for trapped electron modes, TEM), is changed by ±20% the growth rates change by only ± ∼3%. Another indication of the modest role that electron driving terms play is that altering electron collisionality by a factor of two (larger and smaller) modifies the growth

rates by only ± ∼4%. In spite of these small responses to changes in the kinetic electron drive, the nonadiabatic electron treatment enhances the growth rate by 40-60% above the results of calculations with adiabatic electrons and the experimental ratio of T_e/T_i. This kinetic electron enhancement of modes with dominantly ITG characteristics is quite common in tokamaks. The ion temperature profile shape in this i-ITB plasma is far from the threshold for ITG stability. Even with a 50% reduction of a/L_{Ti} the fastest growing modes have an ITG character; in particular, even with this reduced a/L_{Ti}, they respond relatively weakly to changes in a/L_{Te}.

IV. LINEAR STABILITY

Several plasma characteristics change during the time interval simulated here, and the effect of individual parameters on the linear stability is estimated by changing them one at a time in calculations. We also discuss how the evolving conditions may affect the heat transport. The ion heating estimates below are based on TASK3D[40] calculations with slowing down included. As explained in Ref. 6, this type of analysis is needed in order to properly account for the effect of the changing density and neutral beam power. The collisional temperature equilibration power is included in the heating reported here, but is never more than 0.25 MW, and $|dW_i/dt| \leq 0.2$ MW so that also plays a small role.

As shown in Fig. 1, the total injected power is increased by ∼20% at 4.6 sec, but the added P-NB doubles the number of low energy neutral beams and the density increase produced by the pellet leads to a higher deposition rate and faster slowing down than at earlier times. Consequently, the ion heating at 4.74 sec inside r/a=1. and 0.5 is increased by 80% and 90%, respectively, relative to the pre-pellet time of 4.44 sec. At the first simulation time, 4.64 sec, the ion temperature is still rising because it has not had time to reach the level that could be supported by this higher ion heating rate. As both the carbon and electron density continue to decline following pellet injection, the estimated core ion heating falls slowly by about 10% between 4.74 and 4.94 sec, so a portion of the T_i rise and fall is directly related to the changes in ion heating. Power balance analyses[6,7] consistently point to improved ion confinement in the central region of i-ITB plasmas with $r/a \leq$∼0.4. In the region of our simulations, $r/a \geq$0.5, sometimes χ_i (and even $\chi_i/T_i^{3/2}$) rise at the time of peak ion temperature and gradient scale length[6], but in other cases χ_i does not increase

and $\chi_i/T_i^{3/2}$ drops[7] at this time. A detailed quantitative accounting of any changes in ion heat transport requires careful heating calculations that include the time-dependent carbon and electron densities in calculations of the neutral beam ionization and the fast ion slowing down, but these are not currently available.

The frequency and growth rate spectra for all four simulation times are compared in Figs. 10-11 and 12-13 for r/a=0.7 and 0.5, respectively. The GS2 code uses dimensionless frequencies and growth rates normalized by a reference rate, $v_i/a = \sqrt{2T_i/m_H}/a$, that varies from time to time here because the ion temperature is not completely steady. In Figs. 10-13 a fixed reference rate - that for t=4.84 sec - has been used for all times so the curves are directly comparable.

The low growth rates at r/a=0.7 and t=4.64 sec (Fig. 10) are mostly due to the large carbon density at this time, which reduces the density of hydrogen, the main driver of the instability. If the ion density fractions are changed to the values at t=4.84 sec, but all other parameters are kept at the values for t=4.64 sec, the growth rates rise to just below the t=4.84 curve (Fig. 11a). If the value of T_e/T_i at t=4.84 sec is also used, then the growth rates rise to the level at t=4.94 sec for all but the highest $k_y\rho_i$ (Fig. 11b). The elevated carbon density at the earliest time may therefore be primarily responsible for the high T_i at r/a=0.7 and t=4.64 sec.

The large growth rates at r/a=0.7 and t=4.74 sec are caused by the especially high a/L_{Ti} (see Fig. 4), and the invigorated turbulence is presumably a cause of the ion temperature saturation near t=4.7 sec. The rising core T_i has produced a a steeper profile shape and the increased ion heat transport plays a role in halting the temperature rise.

The low growth rates at r/a=0.5 and t=4.64 sec (Fig. 12), are mostly caused by the low a/L_{Ti} at this time and location. By increasing a/L_{Ti} to its value at t=4.84 sec, the growth rates are raised almost fully to the level seen at the later times (see Fig. 13a). Although the carbon density is high at t=4.64 sec, its effect on the growth rate (via hydrogen dilution) is not strong (although it is strong at r/a=0.7) except for the highest $k_y\rho_i$ modes (see Fig. 13b), but they are not expected to make a very important contribution to the ion heat flux. From this analysis, it appears that the ion temperature is still rising at r/a=0.5 and t=4.64 sec because a/L_{Ti} has not yet risen to the point where the transport will balance the recently increased ion heating.

Growth rates for all radii and times are compared in Fig. 14 for modes with $k_y\rho_i$=0.6;

in all cases this is the largest growth rate or is close to it. Here the growth rate is given in kHz to show that it is in the range of the measured density fluctuations, 20-500kHz, shown in Figs 6-7. The largest growth rate occurs at r/a=0.7 and t=4.74 sec, a consequence of the large $a/L_{\rm Ti}$ and large $T_{\rm i}$ (which raises the normalizing reference rate) at this time and location. This is also the only time with a significant radial variation in the growth rate, again owing to the unusual conditions at r/a=0.7. These results are consistent with the measured broad radial profiles of density fluctuation with peaks in the vicinity of $r/a \sim$0.7 (Figs. 6 and 7). In microstability calculations for another i-ITB discharge[17] the location of the peak of the maximum growth rate also roughly corresponds to the peak of the measured fluctuations. The relatively low growth rates at t=4.64 for all three radii might explain the lower measured density fluctuation levels at this time, but we have no explanation for why the observed increase at later times is restricted to the lower half of the plasma (Fig. 6).

V. QUASILINEAR CARBON FLUXES

Our quasilinear estimate of the carbon particle flux begins with GS2's dimensionless flux, $\Gamma_{\rm C}$, which is normalized by a 'reference' flux, $\Gamma_{\rm ref} = (n_{\rm e}/a)\rho_{\rm i}^2 v_{\rm i}/a$. In a linear stability calculation the flux and fluctuating potential grow exponentially, but the ratio of the two becomes stationary and depends on the cross-phase between the fluctuating potential and density and their ratio:

$$\Gamma_{\rm C}/\langle|\delta\phi|^2\rangle \propto sin(\alpha_{\delta\phi,\delta n})\frac{\langle|\delta n|\rangle}{\langle|\delta\phi|\rangle},$$

where GS2's dimensionless fluctuating potential and density are normalized by $T_{\rm e}\rho_{\rm i}/a$, and $n_{\rm e}\rho_{\rm i}/a$, respectively. For low $k_{\rm y}\rho_{\rm i}$ we find that $\Gamma_{\rm C}/\langle|\delta\phi|^2\rangle$ approaches zero, and that is the reason why the weighted fluxes defined next and shown in Figs. 15-17 become small for low $k_{\rm y}\rho_{\rm i}$ (heat fluxes have a similar cutoff, as shown in Fig. 18).

Many quasilinear formulations[41–44] set the magnitude of the turbulent diffusivity with a mixing length estimate, $\gamma/k_\perp^2$, where the *dimensional* quantities are used. A dimensional flux is not needed here, but a similarly motivated (dimensionless) weighting function, $(\gamma a/v_{\rm i})/(k_{\rm y}\rho_{\rm i})^2$, helps define which $k_{\rm y}\rho_{\rm i}$ are important. In order to compare the carbon diffusivities at times with very different carbon densities, we divide the particle flux by the carbon density fraction to produce a quantity proportional to $(D/n_{\rm C})\nabla n_{\rm C}+V \sim Da/L_{\rm nC}+V$ rather

than $D\nabla n_{\rm C} + V n_{\rm C}$. The quasilinear particle flux is then given by

$$\Gamma_{\rm ql,C} = \frac{\Gamma_{\rm C}(n_{\rm e}/n_{\rm C})}{\langle|\delta\phi|^2\rangle}\frac{(\gamma a/v_{\rm i})}{(k_{\rm y}\rho_{\rm i})^2}. \quad (1)$$

Although the peak growth rates are typically at $k_{\rm y}\rho_{\rm i}$=0.6, the particle (and heat flux) spectra peak at $k_{\rm y}\rho_{\rm i}$=0.28 or 0.4 (Figs. 15-18). The downshift is caused by the mixing length weighting function, which rises increasingly steeply as $k_{\rm y}\rho_{\rm i}$ diminishes. In spite of this continuing rise, both the carbon particle flux and the heat fluxes turn over sharply below $k_{\rm y}\rho_{\rm i}$=0.28, which justifies the termination of the spectrum at $k_{\rm y}\rho_{\rm i}$=0.20.

At each of the simulation times and radial locations we vary the carbon density gradient parameter, $a/L_{\rm nC}$, between -1 and +0.15 to search for conditions which produce outward carbon flux. For all four times, all three radii, and all six $k_{\rm y}\rho_{\rm i}$ the quasilinear carbon fluxes are inward when the carbon density is hollow, or $a/L_{\rm nC} < 0$. The fluxes become small only for $a/L_{\rm nC}\sim$0, so the diffusivity dominates the turbulent pinch for these conditions. The results for three cases are discussed below to illustrate these results.

The first simulation time, 4.64 sec, follows the carbon pellet injection by only 90 msec so the carbon density is still high (Fig. 5). Although the pellet injection has suppressed the temperatures, the ion temperature is already elevated at 4.64 sec - and is still rising. Near r/a=0.5 the ion temperature gradient parameter is weakest at this time (Fig. 4), establishing one end of the range covered by this parameter. This time also corresponds to the high end of the carbon density range. The carbon flux spectra for the $a/L_{\rm nC}$ scan are shown in Fig. 15, and there are no outward fluxes produced by hollow carbon density profiles. The measured value is $a/L_{\rm nC}$=-0.9 for this location and time, which is far from what is needed for an outward flux.

The highest ion temperature gradient parameter (and highest core ion temperature) is achieved at 4.74 sec and r/a=0.7. The carbon flux spectra, in Fig. 16, are qualitatively similar to those in Fig. 15, but here even a mildly peaked carbon density, with $a/L_{\rm nC}$=+0.15, produces a small *inward* carbon flux. The measured carbon density is already substantially lower than at 4.64 sec, and the measured $a/L_{\rm nC}$=-0.64 again produces an inward flux.

The final highlighted condition is at 4.94 sec and r/a=0.5, when the ion temperature has decayed below the values of the first two simulation times (Fig. 4) - although the ion temperature gradient parameter is little changed after 4.64 sec - but the impurity hole has deepened dramatically (Fig. 5). We include the measured $a/L_{\rm nC}$=-3.5 for carbon in addition

to the standard values in the $a/L_{\rm nC}$ scan to show that strongly hollow carbon density profiles produce an even larger inward carbon flux (Fig. 17).

At late times the measured carbon profile becomes stationary for $r/a \geq 0.7$, although $a/L_{\rm nC}$ has continued to fall at all three simulation locations (see Fig. 5). As the carbon density approaches steady state conditions the carbon flux must approach zero in the plasma core where there is no source of carbon. The conditions that produce null quasilinear carbon fluxes therefore define the steady state carbon density profile shape consistent with purely turbulent particle transport. Our results indicate that null flux is achieved only with nearly zero carbon density gradient, corresponding to a flat carbon density throughout the radial range of the calculations, $0.5 \leq r/a \leq 0.7$, in disagreement with the profiles in Fig. 5 at later times.

Quasilinear estimates of transport fluxes can be reliable when they are based on nonlinear simulations[42–46]. Saturation of turbulence is governed by *nonlinear* processes that establish the overall magnitude of the turbulence and the relative importance of modes with different perpendicular scale lengths. This is especially important when considering quasilinear estimates of particle flux because partial cancellation of oppositely directed fluxes for different $k_{\rm y}\rho_{\rm i}$ can occur in some situations[45], and then the relative contributions must be accurately known to obtain the correct total flux. Nonlinear turbulence simulations in stellarator geometries are very computationally demanding, however, and the available nonlinear simulations are restricted to a single ion species with adiabatic treatment of electrons (making studies of particle transport impossible) so there are no nonlinear simulations that could guide our quasilinear formulation.

In spite of these circumstances, the results reported here are far from tentative for two reasons. The first is the qualitative nature of the issue to be addressed: is the turbulent flux of carbon outward for plasma parameters in the impurity hole regime? The second reason is that the GS2 fluxes are *universally inward* when the carbon density is flat or hollow so there is no possible weighting function that will produce an outward flux in the impurity hole region. While it is conceivable that a nonlinear simulation could have a cross-phase sufficiently different from the linear calculation to change the sign of the particle flux, there is no precedent for such a large difference between linear and nonlinear cross-phases in the available comparisons of quasilinear and nonlinear fluxes[42–48].

VI. ION HEAT FLUX STIFFNESS

As noted above the ion temperature profile shape in this i-ITB plasma is far from the threshold for ITG stability. Even with a 50% reduction of a/L_{Ti} the fastest growing modes have an ITG character and respond relatively weakly to changes in a/L_{Te}. When combined with the approximately offset-linear character of the a/L_{Ti} dependence of the heat flux, this is produces a relatively low 'stiffness', a desirable characteristic that may be common in stellarators[19,49–51].

A commonly used measure of stiffness is the ratio of two thermal diffusivities[19]: the 'incremental' value often derived from 'heat pulse' analysis, and the 'power balance' value. These may be derived from the dependence of Q/n on ∇T, as illustrated in Fig. 3 of Ref. 19.

The ion heat flux in tokamaks is often rather stiff, with experimental values estimated from various JET conditions in Ref. 52 ranging from 10 (Fig. 2, χ_{s}=7) and 7 (Fig. 2, ρ=0.64) to 3 (Fig. 2, χ_{s}=2) and 2.5 (Fig. 5, the case with high ω with R/L_{Ti}=4.5). Turbulence simulations for tokamaks in Fig. 8 of Ref. 52 have stiffness of 2 from TLGF (see the cases without low shear) and 3 from GYRO, while GYRO simulations produce a stiffness of 2.5 based on Fig. 10 of Ref. 53. We show below that our quasilinear estimate of ion stiffness in the i-ITB regime of LHD is 1.5–2.5, and nonlinear simulations of ITG turbulence in W7-X appear to have relatively low stiffness as well[51].

Low *electron* stiffness is often observed in both tokamaks and stellarators[19,50], but higher values are observed in higher density plasmas in HSX[54]. In several stellarators the measured electron stiffness is below 2, but no experimental values for ion stiffness are available. Experimental estimates of electron stiffness in LHD have been made for e-ITB plasmas[50], but these discharges have much lower ion temperatures and the turbulent transport mechanism must be quite different from the i-ITB plasmas studied here. Our calculated electron stiffness for these conditions is $\sim$1, but the electron heat flux estimates may be seriously incomplete because we neglect ETG turbulence and TEM turbulence on small scales, $k_{\mathrm{y}}\rho_{\mathrm{i}} > 1.35$.

In the present calculations the density and temperature may be taken as constants in a scan of a/L_{Ti}. Constant factors such as $1/n$ or a/T can be removed from or applied to Q/n or ∇T without affecting the value of the derived stiffness, S, so we are free to change variables to, for instance, Q and a/L_{T}. The results at different radii are easily compared by

using the integrated heat fluxes in dimensional units, so we use a quasilinear estimate of the turbulent ion heat transport power (integrated over the surface) in place of Q/n and $a/L_{\rm T}$ in place of ∇T, in the definition of ion stiffness

$$S = \frac{dP_{\rm i}}{d(a/L_{\rm Ti})} \frac{(a/L_{\rm Ti})}{P_{\rm i}}.$$

In the previous section we found that the ratio of the carbon flux to the square of the fluctuating potential is responsible for the small flux contributed by the low wavenumber modes. Here we use the ratio of GS2's dimensionless heat flux and the square of the fluctuating potential, $Q_{\rm i}/\langle|\delta\phi|^2\rangle$, to define the low wavenumber cutoff for modes that contribute significantly to the heat flux. Fig. 18 shows that the mode with $k_{\rm y}\rho_{\rm i}$=0.2 contributes weakly to the heat flux, so we focus attention on the modes with $k_{\rm y}\rho_{\rm i}$=0.28, 0.4, 0.6 since they are expected to make the dominant contributions to the heat flux.

The mixing length estimate for the thermal diffusivity is $\gamma/k_\perp^2$, where the *dimensional* quantities are used. The total turbulent ion heat flux crossing the given surface is obtained by multiplying this diffusivity by the sum of the ion densities, the area of the magnetic surface, and ∇T. The quasilinear ion heat fluxes and the stiffness are shown in Fig. 19 at several locations and times, for $\pm$20% scans of $a/L_{\rm Ti}$ surrounding the measured value. These locations and times are chosen to include extrema of $a/L_{\rm Ti}$ and carbon density as well as typical values of both parameters. As in many other circumstances in tokamaks and stellarators the $a/L_{\rm Ti}$ dependence of $P_{\rm i}$ is approximately 'offset linear', so the stiffness is highest near threshold. The stiffness of the quasilinear ion heat flux is mostly in the range 2.0-2.3 at the experimental $a/L_{\rm Ti}$, although the case at t=4.74 sec and $r/a = 0.7$ has a stiffness as low as 1.7. For a given location and time the stiffness for the three $k_{\rm y}\rho_{\rm i}$ are similar - in spite of the wide variation of the heat fluxes. The chief source of uncertainty for these predictions is the adequacy of the quasilinear approximation; a planned publication on nonlinear turbulence simulations of LHD plasmas will address stiffness.

These quasilinear results are superficially consistent with the experimental analysis of heat flux in an LHD plasma with an ion-ITB[55] that finds the ion stiffness is reduced when the ion-ITB forms. However, close study of that transport analysis reveals a more profound change than suggested by the continuous reduction of stiffness with increased heat flux and ion temperature gradient parameter seen in Fig. 19. During the L-mode phase the ion heat flux doubles while the ion temperature gradient changes very little, while during the

development of the i-ITB the ion heat flux grows rather little while the normalized ion temperature gradient almost doubles (see Figs. 2-3 of Ref. 55). None of the parametric dependences studied here can provide such a dramatic transition, suggesting that the key to the transition lies outside the processes examined here.

VII. SUMMARY

The extremely hollow impurity density profiles, or 'impurity holes', observed in low density LHD plasmas heated by neutral beam injection can not be understood within the context of standard neoclassical transport analysis, which predicts that impurity particle fluxes must be inward in the ion-root regime. We have explored whether microturbulent transport might explain the observed outward fluxes by means of quasilinear transport estimates based on comprehensive linear stability calculations that include hydrogen, helium and carbon, and a kinetic treatment of electrons that includes collisions. The response of the growth rate to variations in temperature- and density-gradient drive terms identifies the dominant microinstabilities as ITG modes at all four times and all three radii studied.

Quasilinear estimates of the carbon particle flux are uniformly inward with hollow carbon profiles, so turbulent transport generated by electrostatic modes with $k_{\rm y}\rho_{\rm i}$ <2 does not provide an explanation for the observed outward flux of impurities in 'impurity hole' plasmas. No alternative mode-weighting choice can alter this conclusion because the quasilinear flux is inward for all mode wavenumbers studied here. Nonlinear simulations could overturn this conclusion only if they reverse the sign of the cross-phase between the fluctuating potential and density, a hypothetical possibility that is without precedent. There is usually a close correspondence between the linear and nonlinear cross-phase[42–48]. It is possible that other forms of turbulent transport may produce different results; the present simulations are limited to ion-scale electrostatic turbulence. Perhaps electromagnetic modes will produce the needed fluxes (in spite of the modest β of these plasmas), but these modes have been excluded from this study to reduce the computational cost.

An explanation of the impurity hole phenomenon might be found within neoclassical transport theory, but this has not yet been achieved and some features are quite challenging. The electrostatic potential is predicted to have poloidal variation which will contribute to the radial drift, and while this often–neglected drift is small compared to the curvature and

$\nabla|B|$ drifts for low Z ions, it could be important for carbon and higher-Z impurities[11,12]. Although initial calculations that include these previously neglected terms indicate that the impurity particle fluxes are significantly affected and that it is possible to produce outward impurity flux in the ion-root regime in the LHD configuration[12], the density and temperature profiles assumed in Ref. 12 are much more collisional than those of the impurity hole regime. Recent calculations with parameters much closer to impurity hole conditions have not produced results that can explain the outward fluxes that create the impurity hole[13], but the calculation method is still under development so it is too early to draw definite conclusions. If the radial electric field were positive then the neoclassical flux could be outward, but this explanation is restricted to the outer part of the plasma because measurements with the heavy ion beam probe show that the radial electric field is negative for r/a <0.55[4,5]. Based on plasma flow measurements, the radial electric field is positive near the plasma edge[5], but there is a measurement gap where the carbon's hollow density gradient is steepest and it is most important to understand why the carbon flux is outward. An additional challenge to theory is the sudden reversal (see Fig. 1 of Ref.1) from carbon accumulation to expulsion: why should small changes in driving gradients produce such a dramatic convective reversal?

The stiffness of the quasilinear ion heat flux is found to be mostly in the range 2.0-2.3 at the experimental a/L_{Ti}, but for the conditions at t=4.74 sec and $r/a = 0.7$ stiffness may be as low as 1.7. These results are consistent with the experimental analysis of heat flux in an LHD plasma with an ion-ITB[55] that finds the ion stiffness is suddenly reduced when the ion-ITB forms, and this follows a very different L-mode phase when the plasma appears to be quite stiff: the ion heat flux doubles while the ion temperature gradient changes very little.

We thank M. Yokoyama for TASK3D analysis, and C.D. Beidler, G.W. Hammett and P. Xanthopoulos for helpful discussions. This work has been done under the collaboration research of National Institute for Fusion Science. It is a pleasure to acknowledge cooperation and discussions with Professors K. Komori, O. Kaneko and H. Yamada of National Institute for Fusion Science. This work was supported by U.S. Department of Energy Contract No. DE-AC02-76CH03073. This research used resources of the National Energy Research Scientific Computing Center (NERSC), which is supported by the Office of Science of the U.S. Department of Energy under Contract No. DE-AC02-05CH11231. Use of parallel

computer clusters at PPPL is also gratefully acknowledged.

REFERENCES

[1]K. Ida *et al.*, Phys. Plasmas **16**, 056111 (2009).

[2]M. Yoshinuma *et al.*, Nucl. Fusion **49**, 062002 (2009).

[3]M. Yoshinuma *et al.*, "Impurity transport of ion-ITB plasmas on LHD, EXC/9-1," (October 2010), IAEA Fusion Energy Conference, Seoul.

[4]T. Ido *et al.*, Plasma Phys. & Controlled Fusion **52**, 124025 (2010).

[5]K. Nagaoka *et al.*, Nucl. Fusion **51**, 083022 (2011).

[6]H. Lee *et al.*, Plasma Phys. & Controlled Fusion **55**, 014011 (2013).

[7]H. Takahashi *et al.*, Nucl. Fusion **53**, 073034 (2013).

[8]A. Iiyoshi *et al.*, Nucl. Fusion **39**, 1245 (1999).

[9]Y. Nakamura, NIFS, (2014), private communication.

[10]H. Maassberg *et al.*, Plasma Phys. & Controlled Fusion **41**, 1135 (1999).

[11]C. D. Beidler and H. Maassberg, "Implications of the quasi-neutrality condition for neoclassical transport in stellarators," (2005), 15th International Stellarator Workshop (Madrid, 3-7 October) poster P2-02,http://www-fusion.ciemat.es/SW2005/conferences/madrid06/proceedings/posters/(P2-02)_BeidlerCD.pdf.

[12]J. M. Garcia-Regaña *et al.*, Plasma Phys. & Controlled Fusion **55**, 074008 (2013).

[13]J. M. Garcia-Regaña, IPP, (2014), private communication.

[14]G. Rewoldt *et al.*, Nucl. Fusion **42**, 1047 (2000).

[15]O. Yamagishi *et al.*, Phys. Plasmas **14**, 012505 (2007).

[16]K. Tanaka *et al.*, "Density profile and microturbulence in LHD," (2012), NIFS Annual Report for 2011-2012, http://www.nifs.ac.jp/report/annrep.html.

[17]M. Nunami, T.-H. Watanabe, H. Sugama, and K. Tanaka, Plasma Fusion Res. **6**, 1403001 (2011).

[18]M. Nunami, T.-H. Watanabe, H. Sugama, and K. Tanaka, Phys. Plasmas **19**, 042504 (2012).

[19]F. Ryter, R. Dux, P. Mantica, and T. Tala, Plasma Phys. & Controlled Fusion **52**, 124043 (2010).

[20]N. A. Pablant *et al.*, Rev. Sci. Instrum. **83**, 083506 (2012).

[21]M. Yoshinuma *et al.*, Fusion Sci. Technol. **58**, 375 (2010).

[22]M. Goto *et al.*, Phys. Plasmas **10**, 1042 (2003).

[23]S. Morita *et al.*, Plasma Fusion Res. **3**, S1037 (2008).

[24]I. Yamada *et al.*, Rev. Sci. Instrum. **81**, 10D522 (2010).

[25]K. Tanaka *et al.*, Plasma Fusion Res. **3**, 050 (2008).

[26]K. Tanaka *et al.*, Rev. Sci. Instrum. **79**, 10E702 (2008).

[27]K. Tanaka *et al.*, Plasma Fusion Res. **5**, S2053 (2010).

[28]M. Kotschenreuther, G. Rewoldt, and W. M. Tang, Comp. Phys. Comm. **88**, 128 (1995).

[29]W. Dorland, F. Jenko, M. Kotschenreuther, and B. N. Rogers, Phys. Rev. Lett. **85**, 5579 (2000).

[30]J. A. Baumgaertel *et al.*, Phys. Plasmas **18**, 122301 (2011).

[31]J. A. Baumgaertel, "Simulating the effects of stellarator geometry on gyrokinetic drift-wave turbulence," (September 2012), Ph.D. dissertation, Princeton University.

[32]G. Rewoldt, L.-P. Ku, W. M. Tang, and W. A. Cooper, Phys. Plasmas **6**, 4705 (1999).

[33]F. Jenko, W. Dorland, M. Kotschenreuther, and B. N. Rogers, Phys. Plasmas **7**, 1904 (2000).

[34]P. Xanthopoulos, F. Merz, T. Görler, and F. Jenko, Phys. Rev. Lett. **99**, 035002 (2007).

[35]M. Nunami, T.-H. Watanabe, and H. Sugama, Plasma Fusion Res. **5**, 016 (2010).

[36]M. A. Beer, S. C. Cowley, and G. W. Hammett, Phys. Plasmas **2**, 2687 (1995).

[37]W. A. Cooper, Plasma Phys. & Controlled Fusion **34**, 1011 (1992).

[38]P. Xanthopoulos *et al.*, Phys. Plasmas **16**, 082303 (2009).

[39]S. P. Hirshman and O. Betancourt, J. Comput. Phys. **96**, 99 (1991).

[40]M. Yokoyama *et al.*, Plasma Fusion Res. **8**, 2403016 (2013).

[41]M. Kotschenreuther, W. Dorland, M. A. Beer, and G. W. Hammett, Phys. Plasmas **2**, 2381 (1995).

[42]F. Jenko, T. Dannert, and C. Angioni, Plasma Phys. & Controlled Fusion **47**, B195 (2005).

[43]J. Kinsey *et al.*, Phys. Plasmas **15**, 055908 (2008).

[44]A. Casati *et al.*, Nucl. Fusion **49**, 085012 (2009).

[45]C. Angioni *et al.*, Phys. Plasmas **16**, 060702 (2009).

[46]T. Hein, C. Angioni, E. Fable, and J. Candy, Phys. Plasmas **17**, 102309 (2010).

[47]F. Merz and F. Jenko, Phys. Rev. Lett. **100**, 035005 (2008).

[48]T. Görler *et al.*, Phys. Plasmas **15**, 102508 (2008).

[49]F. Ryter *et al.*, Plasma Phys. & Controlled Fusion **48**, B453 (2006).

[50]S. Inagaki *et al.*, Nucl. Fusion **46**, 133 (2006).

[51]P. Xanthopoulos *et al.*, "Properties and scaling of gyrokinetic ITG turbulence in stellarator configurations," (2013), 19th International Stellarator-Heliotron Workshop (Padova, 16-20 September) invited talk IS6.

[52]P. Mantica *et al.*, Plasma Phys. & Controlled Fusion **53**, 124033 (2011).

[53]F. Ryter *et al.*, Nucl. Fusion **51**, 113016 (2011).

[54]G. M. Weir *et al.*, "Heat pulse propagation experiments on the HSX stellarator," (2013), 19th International Stellarator-Heliotron Workshop (Padova, 16-20 September) invited talk IS1, http://www.igi.cnr.it/ish_rfp_ws2013/system/files/Weir_ISH_RFP_2013.pdf.

[55]K. Ida *et al.*, Phys. Rev. Lett. **111**, 055001 (2013).

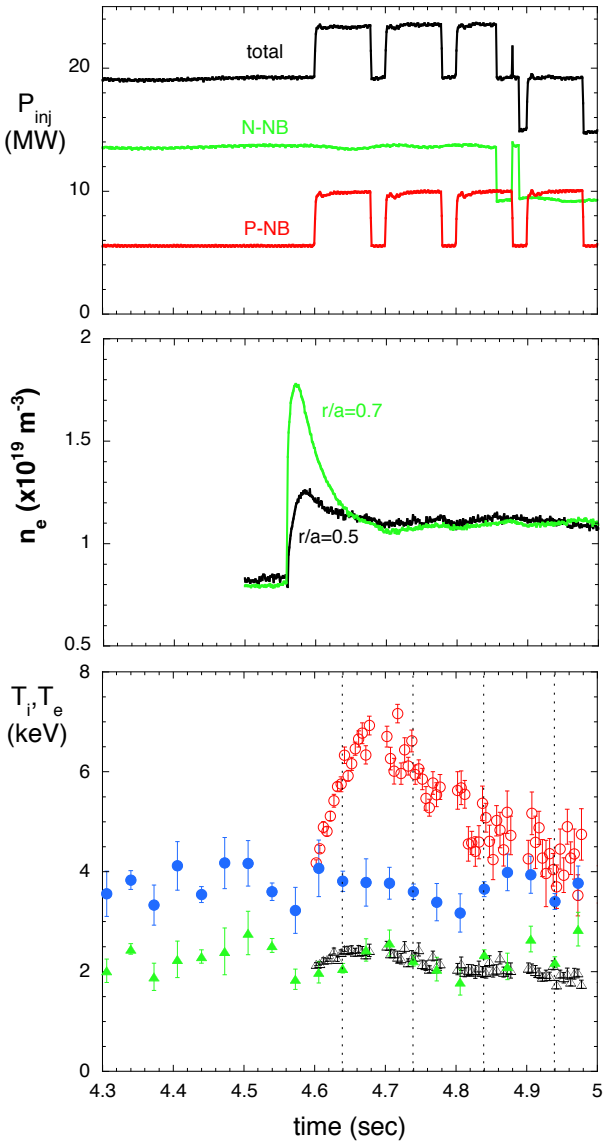

FIG. 1. Injected neutral beam power (port-through power); electron density at r/a=0.5 and 0.7; temperature at r/a=0 (circles) and 0.7 (triangles), filled symbols for electrons, outline symbols for ions. The four vertical dashed lines denote the simulation times.

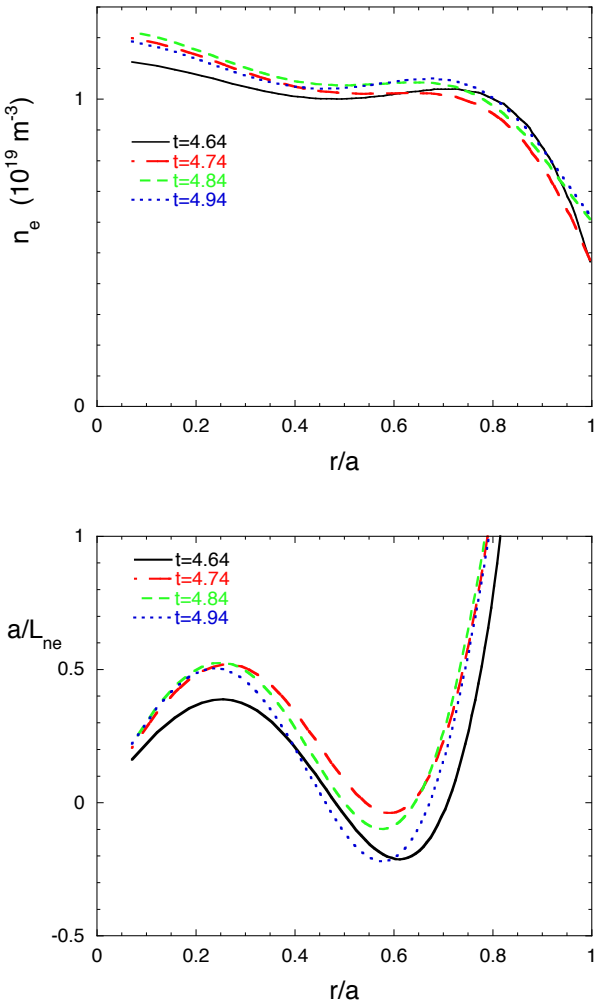

FIG. 2. At four simulation times, profiles of a) electron density and b) electron density gradient parameter.

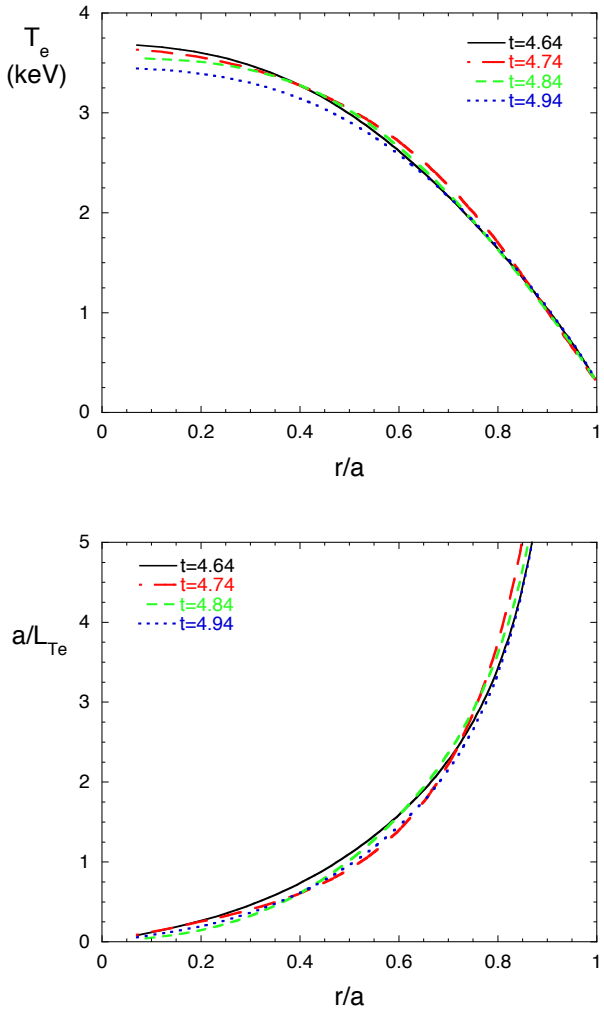

FIG. 3. At four simulation times, profiles of a) electron temperature and b) electron temperature gradient parameter.

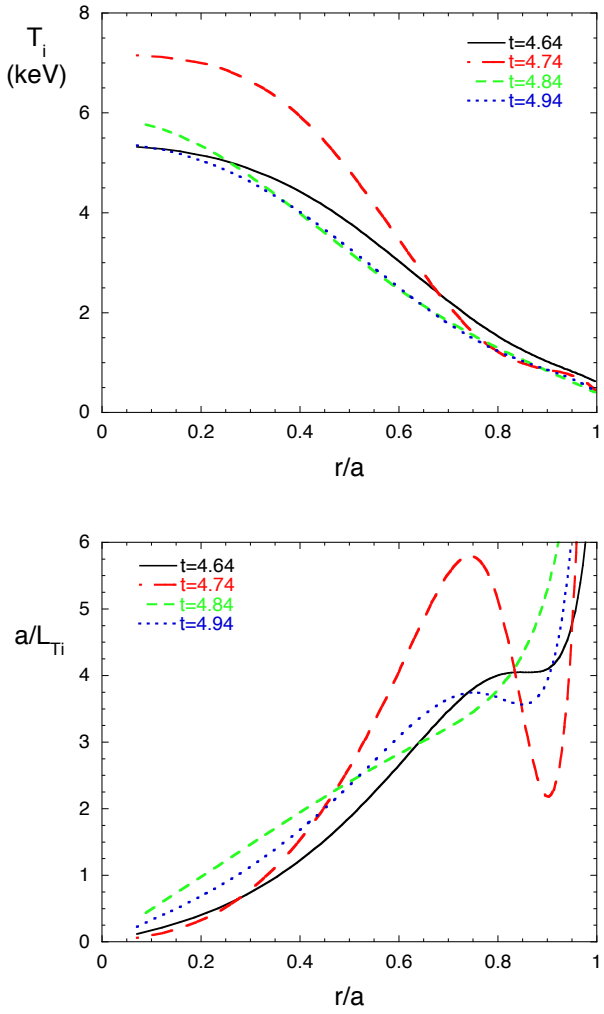

FIG. 4. At four simulation times, profiles of a) ion temperature and b) ion temperature gradient parameter.

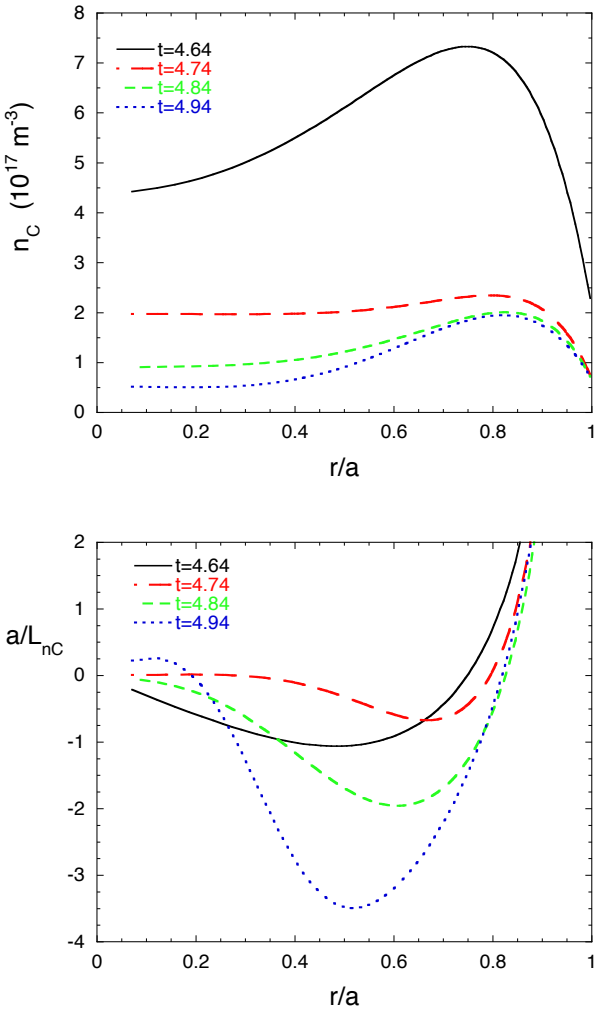

FIG. 5. At four simulation times, profiles of a) carbon density and b) carbon density gradient parameter.

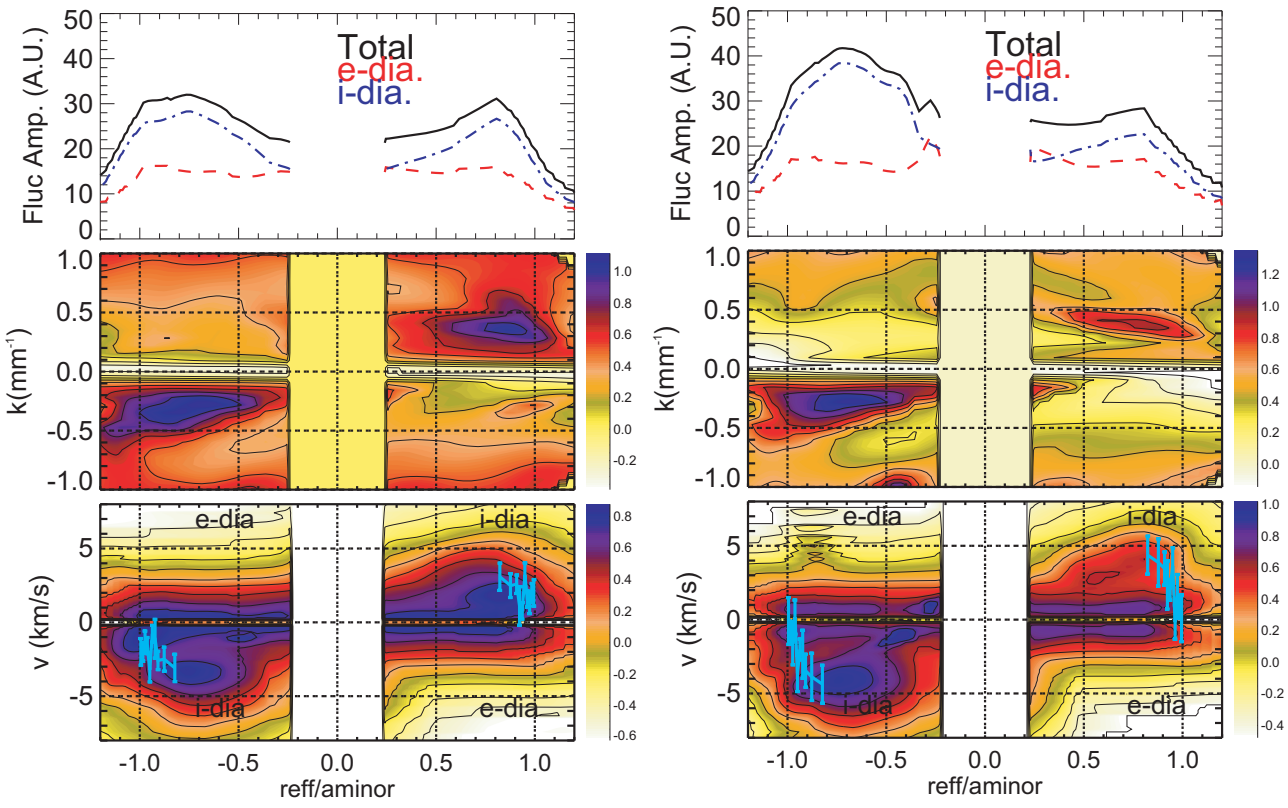

FIG. 6. For t=4.64 (left) and 4.74 sec (right), radial profiles of density fluctuations moving in electron- and ion-diamagnetic directions (see lowest plots) in the lower and upper half of the plasma cross section; contour plots with a logarithmic scale of fluctuation intensity as a function of wavenumber and radial location; and contour plots of fluctuation intensity as a function of phase velocity and radial location. The wavenumber, k, is the poloidal wavenumber, v is the phase velocity in the laboratory frame. Light blue curves with error bars in the phase velocity-r/a plots represent the $E \times B$ poloidal rotation velocity, $v_{\mathrm{E\times B}}$, in the laboratory frame. Labels "i-dia" and "e-dia" in the lowest plots indicate the directions of ion diamagnetic and electron diamagnetic rotation in the laboratory frame, respectively.

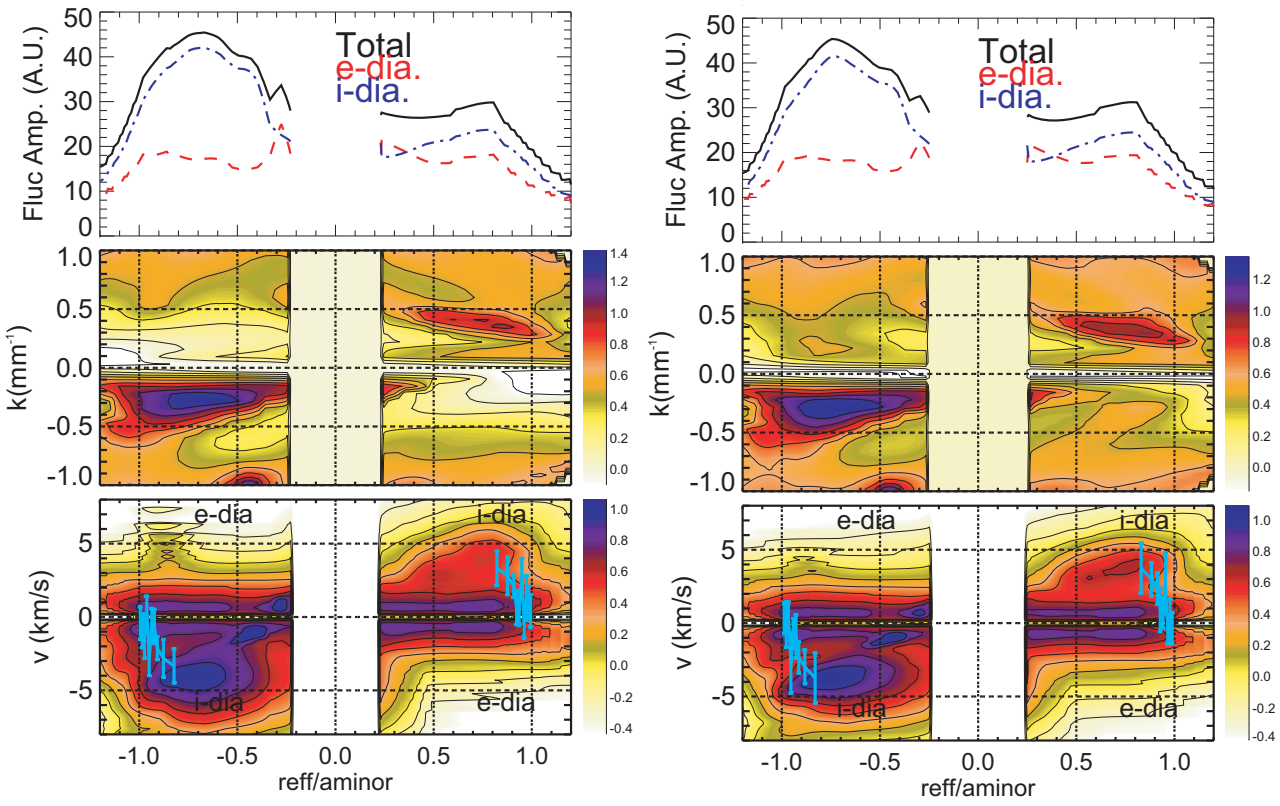

FIG. 7. For t=4.84 (left) and 4.94 sec (right), radial profiles of density fluctuations moving in electron- and ion-diamagnetic directions in the lower and upper half of the plasma cross section; contour plots with a logarithmic scale of fluctuation intensity as a function of wavenumber and radial location; and contour plots of fluctuation intensity as a function of phase velocity and radial location. Definitions are in the caption of Fig. 6.

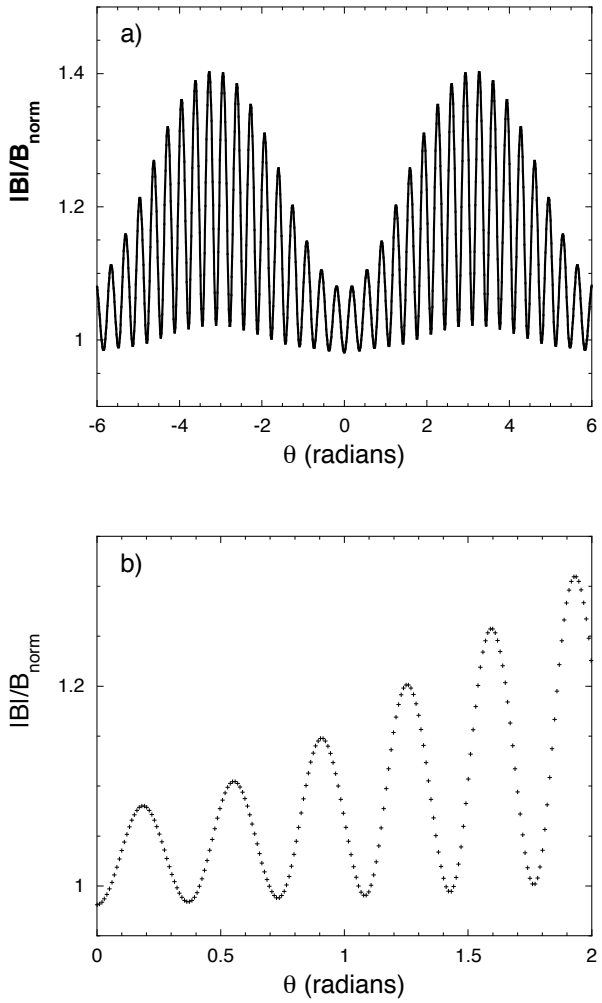

FIG. 8. a) Normalized magnetic field strength for approximately two full poloidal circuits. The outboard midplane is located at $\theta = 0$, the inboard midplane is at approximately $\theta = \pm\pi$. b) Closeup of the grid resolution in several local ripple wells.

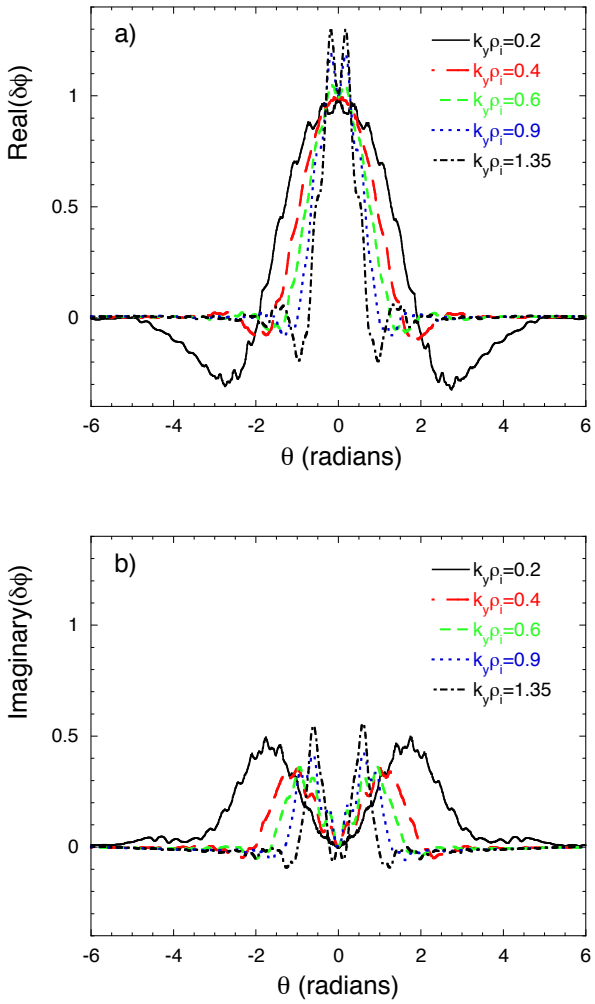

FIG. 9. For r/a=0.6 at t=4.64 sec, the eigenfunctions of the fluctuating potential: a) real part, b) imaginary part. For each $k_{\rm y}\rho_{\rm i}$ the eigenfunction is normalized to make Real($\delta\phi$)=1 at $\theta = 0$.

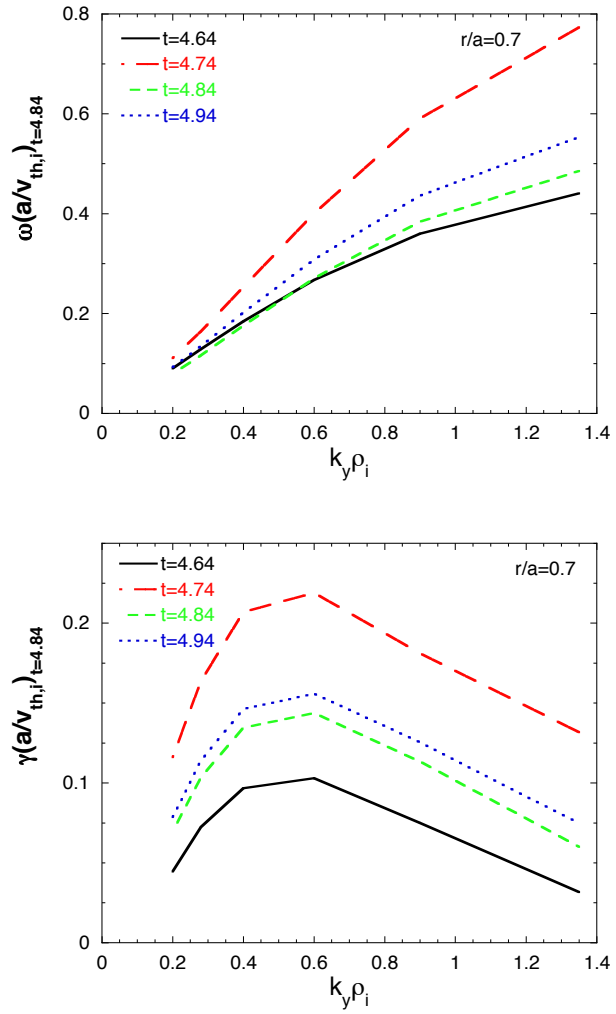

FIG. 10. Normalized frequency spectra and growth rate spectra for r/a=0.7 at t=4.64 sec (solid), 4.74 sec (long dashes), 4.84 sec (short dashes), and 4.94 sec (very short dashes). The normalizing rate for t=4.84 sec is used for all times.

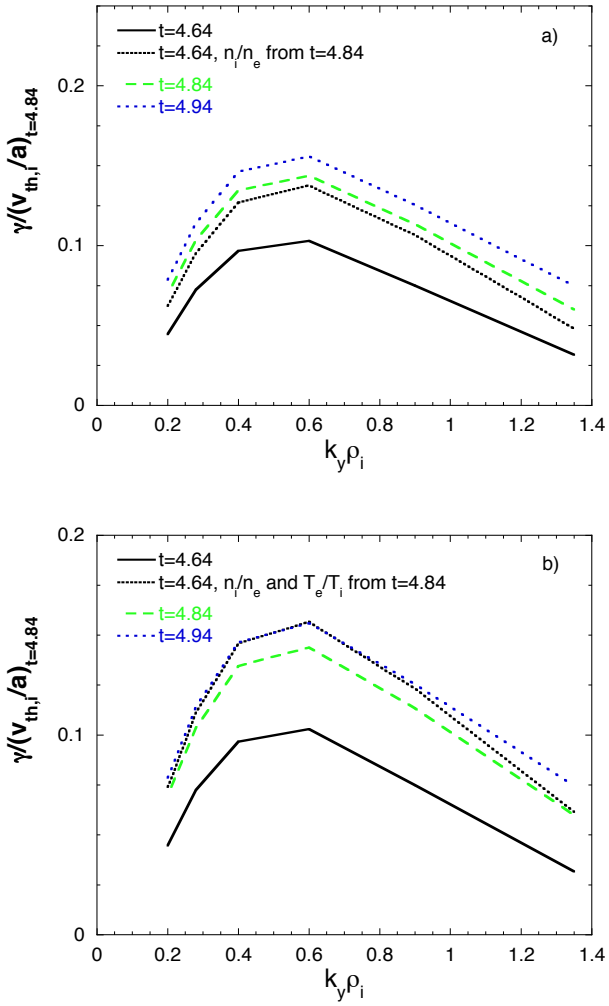

FIG. 11. Normalized frequency spectra and growth rate spectra for r/a=0.7 at t=4.64 sec (solid), modified 4.64 sec (dotted), 4.84 sec (short dashes), and 4.94 sec (very short dashes). In a) the modified t=4.64 sec calculation uses ion density fractions from t=4.84 sec; in b) the temperature ratio is also taken from t=4.84 sec. The normalizing rate for t=4.84 sec is used for all times.

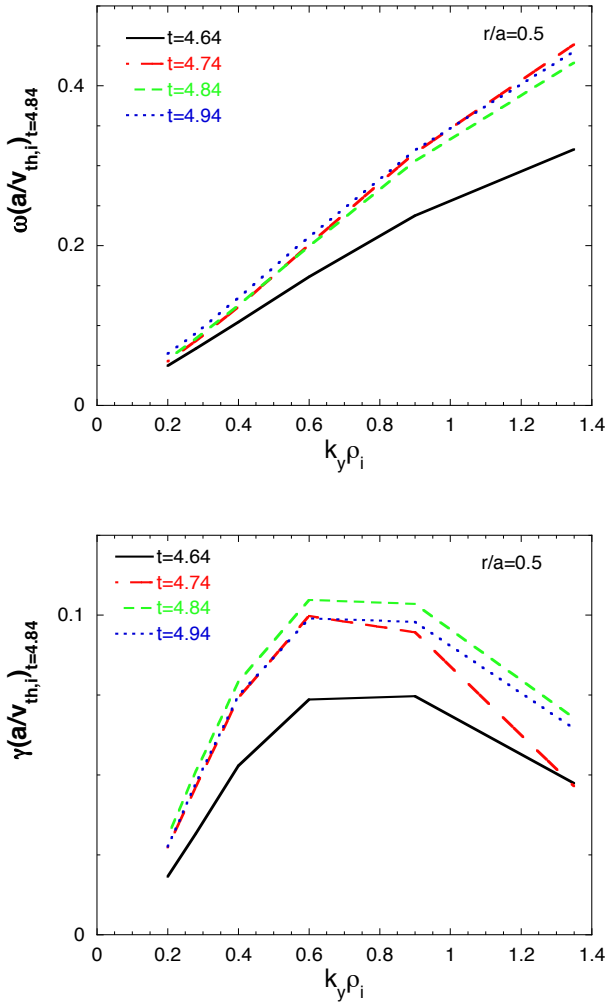

FIG. 12. Normalized frequency spectra and growth rate spectra for r/a=0.5 at t=4.64 sec (solid), 4.74 sec (long dashes), 4.84 sec (short dashes), and 4.94 sec (very short dashes). The normalizing rate for t=4.84 sec is used for all times.

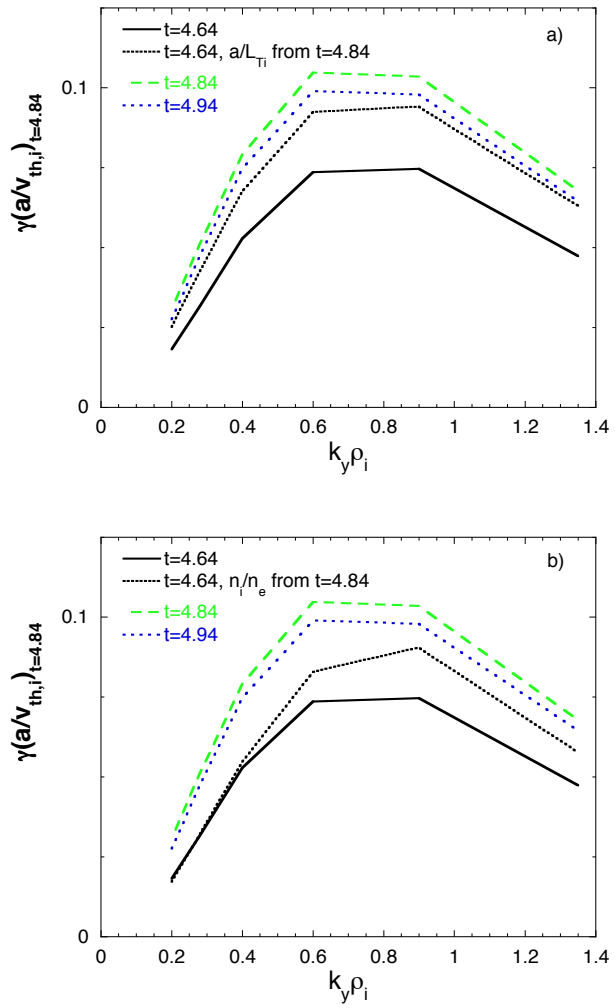

FIG. 13. Normalized frequency spectra and growth rate spectra for r/a=0.5 at t=4.64 sec (solid), modified 4.64 sec (dotted), 4.84 sec (short dashes), and 4.94 sec (very short dashes). In a) the modified t=4.64 sec calculation uses $a/L_{\rm Ti}$ from t=4.84 sec; in b) the ion density fractions are taken from t=4.84 sec. The normalizing rate for t=4.84 sec is used for all times.

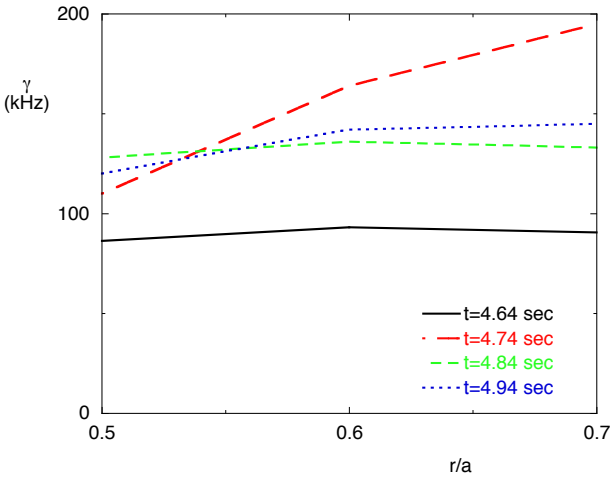

FIG. 14. Growth rate vs. radius for mode with $k_y\rho_i$=0.6; at t=4.64 sec (solid), 4.74 sec (dashed), 4.84 sec (short dashes), and 4.94 sec (very short dashes).

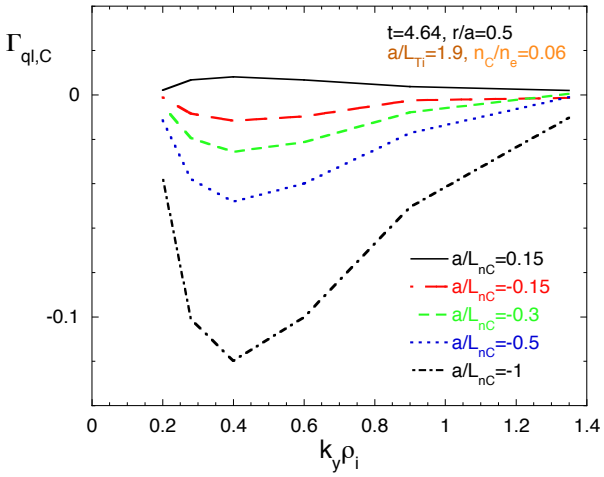

FIG. 15. For t=4.64 sec and r/a=0.5, spectra of the quasilinear carbon particle flux (Eq. 1) for five values of the carbon density gradient parameter. Negative values of $a/L_{\rm nC}$ correspond to hollow density profiles, and negative flux corresponds to inward flux. The experimental value of $a/L_{\rm nC}$ is -1.06.

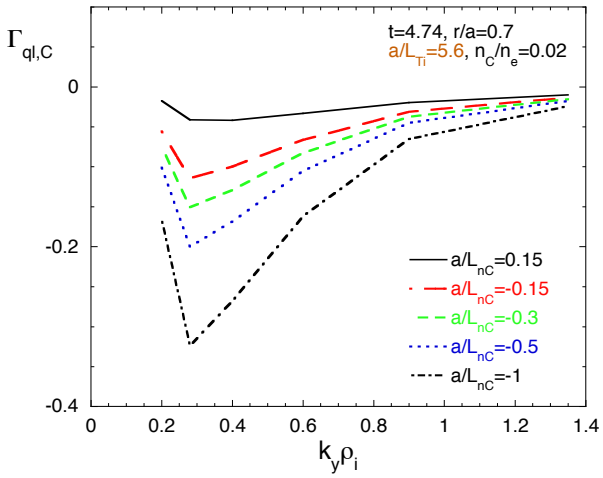

FIG. 16. For t=4.74 sec and r/a=0.7, spectra of the quasilinear carbon particle flux (Eq. 1) for five values of the carbon density gradient parameter. Negative values of $a/L_{\rm nC}$ correspond to hollow density profiles, and negative flux corresponds to inward flux. The experimental value of $a/L_{\rm nC}$ is -0.6.

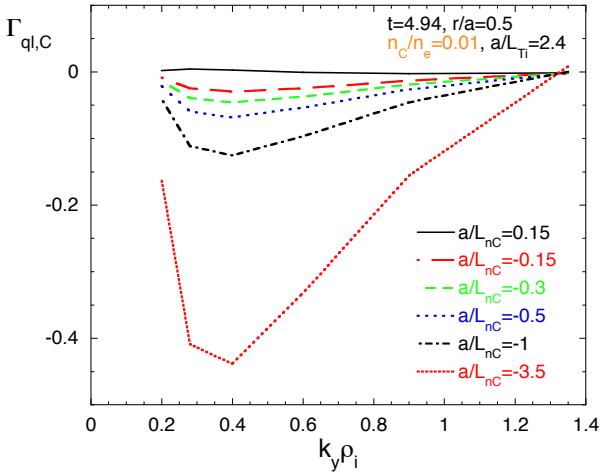

FIG. 17. For t=4.94 sec and r/a=0.5, spectra of the quasilinear carbon particle flux (Eq. 1) for six values of the carbon density gradient parameter. Negative values of $a/L_{\rm nC}$ correspond to hollow density profiles, and negative flux corresponds to inward flux. The experimental value of $a/L_{\rm nC}$ is -3.5.

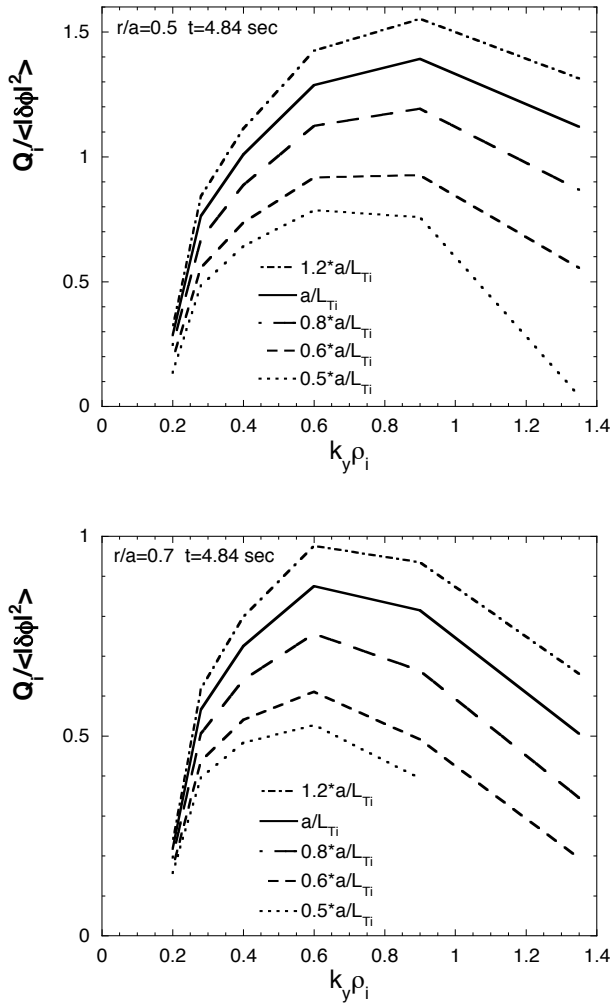

FIG. 18. For r/a=0.5 and 0.7, at t=4.84 sec, the GS2 dimensionless ion heat flux divided by the average value of the square of the fluctuating potential for five values of the ion temperature gradient parameter.

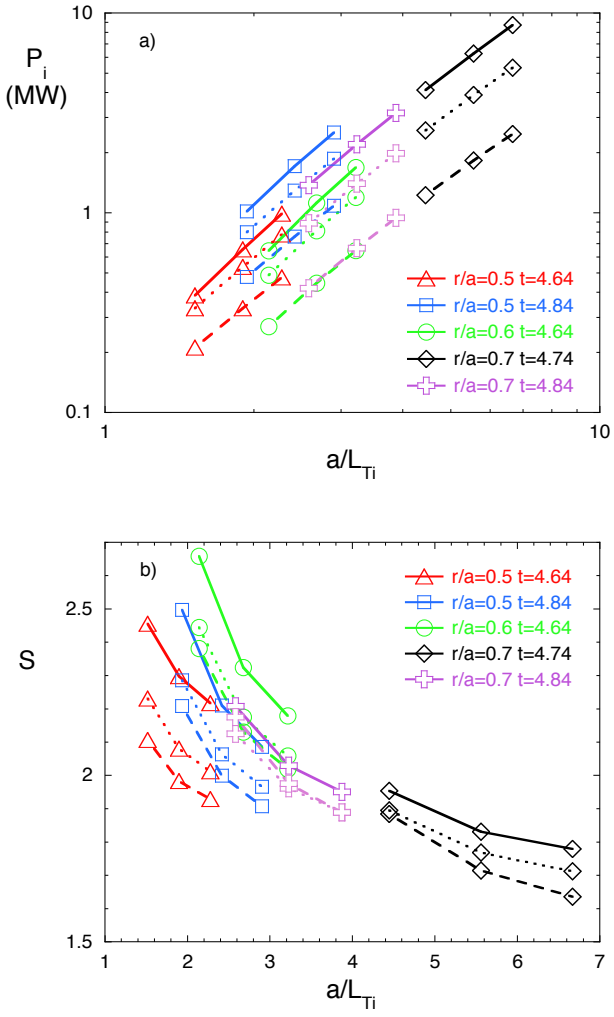

FIG. 19. For scans of $a/L_{\rm Ti}$, a) quasilinear ion heat flux, and b) stiffness vs. ion temperature gradient parameter. In each triplet the central value of $a/L_{\rm Ti}$ is the measured value; the others vary by ±20%. Symbols denote radial location and time: triangle for r/a=0.5, t=4.64 sec; square for r/a=0.5, t=4.84 sec; circle for r/a=0.6, t=4.64 sec; diamond for r/a=0.7, t=4.74 sec; plus for r/a=0.7, t=4.84 sec. Line type denotes the value of $k_{\rm y}\rho_{\rm i}$: solid for $k_{\rm y}\rho_{\rm i}$=0.28, dashed for 0.4, dotted for 0.6.

The Princeton Plasma Physics Laboratory is operated
by Princeton University under contract
with the U.S. Department of Energy.

Information Services
Princeton Plasma Physics Laboratory
P.O. Box 451
Princeton, NJ 08543

Phone: 609-243-2245
Fax: 609-243-2751
e-mail: pppl_info@pppl.gov
Internet Address: http://www.pppl.gov